Solar RRL

RESEARCH ARTICLE OPEN ACCESS

The Role of Halogen-Free Solvents on the Stability of PTQ-2F:BTP-4F-Based Organic Solar Cells

Lukas V. Spanier[1] | Renjun Guo[2,3] | Julian E. Heger[1] | Matthias Schwartzkopf[4] | Stephan V. Roth[4,5] | Peter Müller-Buschbaum[1]

[1]Chair for Functional Materials, Department of Physics, TUM School of Natural Sciences, Technical University of Munich, Garching, Germany | [2]Institute of Microstructure Technology (IMT), Karlsruhe Institute of Technology (KIT), Karlsruhe, Germany | [3]Light Technology Institute (LTI), Karlsruhe Institute of Technology (KIT), Karlsruhe, Germany | [4]Deutsches Elektronen-Synchrotron DESY, Hamburg, Germany | [5]Department of Fibre and Polymer Technology, KTH Royal Institute of Technology, Stockholm, Sweden

Correspondence: Peter Müller-Buschbaum (muellerb@ph.tum.de)

Received: 10 October 2025 | **Revised:** 10 December 2025 | **Accepted:** 26 December 2025

Keywords: aging | morphology | organic solar cell | solvents | stability

ABSTRACT

The appeal of organic solar cells (OSCs) as a source of environmentally friendly electricity is often negatively impacted by the common use of hazardous materials in their manufacturing, such as halogenated solvents. This study explores the fabrication and operational stability of PTQ-2F:BTP-4F-based OSCs using halogenated (chloroform (CF), chlorobenzene) and nonhalogenated (*ortho*-xylene (*o*XY), 1,2,4-trimethylbenzene) solvents in a hot-solvent spin-coating process. Initial power conversion efficiencies (PCEs) of up to 12.2% (CF) and 10.0% (*o*XY) are achieved, with detailed morphological and performance analyses conducted via ex situ and operando grazing-incidence small-angle X-ray scattering (GISAXS). Ex situ measurements reveal significant differences in bulk-heterojunction nanostructures, with benzene-based solvents producing domain size distributions distinct from CF-processed films. Operando GISAXS connects real-time degradation kinetics to the domain size evolution, highlighting solvent-dependent kinetics. Halogenated solvents facilitate a gradual PCE decay, while nonhalogenated solvents exhibit a rapid initial burn-in phase followed by stabilization, with *o*XY-processed OSCs demonstrating superior long-term stability. Morphological stability in *o*XY films originates from the limited coalescence of small polymer domains, retaining a more fine-grained structure in the active layer. This study emphasizes the critical role of processing solvents in OSC performance and stability, positioning *o*XY as a sustainable candidate for scalable and eco-friendly OSC fabrication.

1 | Introduction

Organic solar cells (OSCs) represent a promising solar energy conversion technology, with rapidly increasing power conversion efficiencies (PCEs). Especially the development of novel materials, such as the relatively recent advent of nonfullerene small molecules as acceptor materials in OSCs, has kick-started a rapid increase in new efficiency records in the field of organic photovoltaics [1]. Furthermore, improvements in the bulk-heterojunction (BHJ) morphology and device engineering further enhanced PCEs, now reaching up to 20.82% [2–4]. Such improvements put this emerging technology into direct competition with established inorganic photovoltaic technologies, which are already deployed in a wide range of different implementations in terrestrial as well as space applications [5, 6]. In particular, OSCs are promising for new application areas due to their lightweight and flexible properties, which result in high energy densities being of particular interest to space usage. When going into real-world applications and mass production, potential environmental impacts from the fabrication of OSCs become more relevant, putting focus on harmful halogenated solvents commonly used in the device fabrication process. Traditionally, chloroform (CF) and chlorobenzene (CB) have been utilized most frequently in high-efficiency OSCs [7–9]. However, due to their inherent environmental and health hazards, the interest in using nonhalogenated

solvents such as tetrahydrofuran (THF), *ortho*-xylene (*o*XY), and 1,2,4-trimethylbenzene (TMB) is increasing for manufacturing the BHJ in OSCs [10–13]. This development has sparked considerable research efforts in new derivatives of the now popular small-molecule acceptor (SMA) BTP-4F (also commonly referred to as Y6) to increase its solubility in those nonhalogenated solvents. It is leading to a growing number of different SMA varieties with different alkane sidechains, which impact the morphology of the BHJ, thereby affecting the performance and stability of the resulting solar cells [4, 14–18]. This additional complexity from sidechain engineering can increase manufacturing costs, which, despite low material consumption in OSCs, can lead to high total costs. The usage of less complexly structured molecules and polymers, such as PTQ-2F (also commonly referred to as PTQ10, Figure 1b), can be a way to balance device fabrication costs with achievable PCEs [19, 20], which, for real-world applications of OSCs, turns into an interest-gaining research direction. In conjunction with stability, the simplicity of the fabrication of the OSCs will commercially outperform record-setting donor–acceptor combinations.

Previous work demonstrated the viability of using hot solvents to increase the solubility of BTP-4F in solvents other than CF for slot-die coating BHJs of PBDB-T-2F:BTP-4F, thereby allowing for the scalable fabrication of efficient OSCs from these so-called "green" solvents [10]. This finding also highlights the impact of drying kinetics on the aggregation of the domains within the BHJ, which is a key aspect for obtaining highly efficient OSCs, typically fine-tuned by the inclusion of additives within the solvent [9, 21], which, however, again increases complexity and fabrication costs. In the case of some green solvents, especially those where the solubility of the acceptor is limited due to a comparatively low boiling point, such as 2-methyltetrahydrofuran, the necessary solubility of the acceptor material often can be achieved by engineering the properties of alkyl side chains [7, 12, 22]. Alternative techniques to exert control over the OSCs morphology, such as multistep "layer-by-layer" deposition methods, also increase manufacturing complexity [23, 24].

In this work, we fabricate PTQ-2F:BTP-4F OSCs using both halogenated and nonhalogenated solvents in a hot-solvent spin-coating process. Thus, we focus on a simple OSC system, which is less sensitive compared with recent record-setting donor–acceptor combinations. We investigate the impact of the solvent used on their mesoscopic morphology after fabrication and during device operation. Spin-coated active layers from CF, CB, *o*XY, and TMB result in efficiencies of up to 12.2%, 10.5%, 10.0%, and 9.9%, respectively. We subsequently investigate the time-dependent performance and morphology degradation under illumination by operando grazing-incidence small-angle X-ray scattering (GISAXS), demonstrating a strong influence of the solvent used on the aging behavior of the resulting OSCs. These techniques also allow us to understand the kinetic processes occurring during the operation from degradation by connecting changes in the morphology and performance. Overall, solar cells manufactured from *o*XY demonstrate the highest retention in efficiency, demonstrating the promising potential of this green solvent for the manufacturing of efficient OSCs for commercial applications.

2 | Results and Discussion

2.1 | Ex Situ Analysis

A model solar cell architecture with an inverted device architecture of ITO/ZnO/PTQ-2F:BTP-4F/MoO_3/Ag is selected for this work, which is reported to achieve up to 14.2% of PCE in the literature [25]. The structure of the active layer materials PTQ-2F and BTP-4F is shown in Figure 1b. Apart from CF as an established solvent for PTQ-2F:BTP-4F-based OSCs, CB, *o*XY, and TMB are selected due to their high boiling points (132°C, 143°C, and 168°C, respectively), achieving good solubility for both PTQ-2F and BTP-4F at 80°C, 100°C, and 110°C, respectively (Figure 1a). This is especially relevant for the BTP-4F SMA, which, based on the Hansen solubility parameters (Table S3), has the relative energy difference (RED) at room temperature increased from 0.50 in CF to 0.86, 0.55, and 0.80 in CB, *o*XY, and TMB,

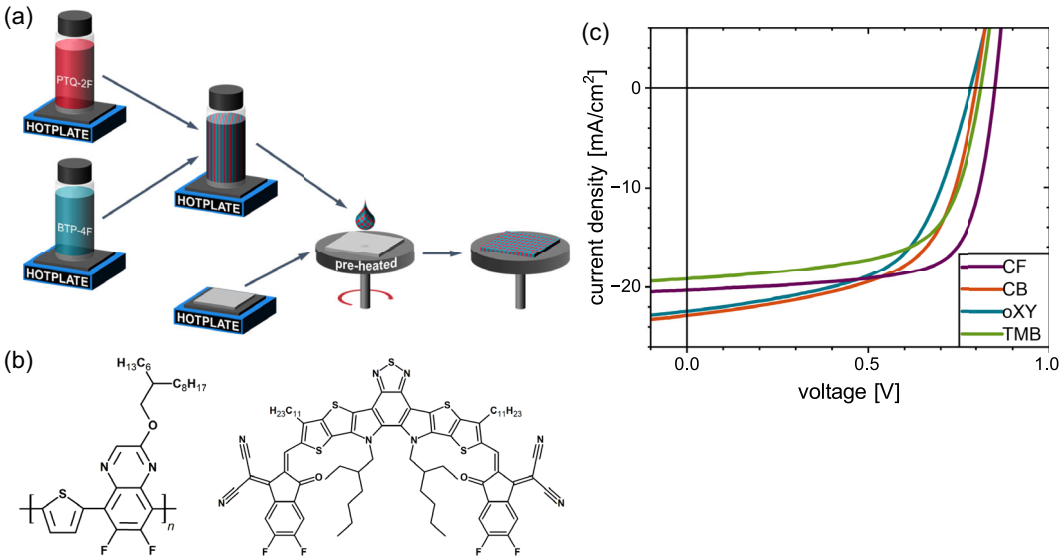

FIGURE 1 | (a) Schematic depiction of the hot spin-coating process. (b) Structural formula of the used materials PTQ-2F and BTP-4F. (c) *J*–*V* curves of champion devices of PTQ-2F:BTP-4F OSCs prepared from different solvents under an AM 1.5G, 100 mW cm^{-2} illumination.

respectively, negatively impacting solubility severely, a trend persisting for similar "Y-series" SMAs [26]. However, the PTQ-2F donor solubility shows little to no adverse influence from these solvents, with the RED calculated at 0.78, 0.63, 0.64, and 0.79 for CF, CB, *o*XY, and TMB, respectively. The preheated solvents also facilitated good drying kinetics during spin-coating, resulting in a smooth, homogenous active layer. THF, despite being a popular green solvent for OSC fabrication, cannot be used in this study due to its low boiling point (65°C) and thus lacks the capability of being heated to obtain sufficient solubility of BTP-4F.

The device performance parameters are summarized in Table 1, with CF-processed devices showing the highest PCE values, followed by CB, *o*XY, and TMB. To investigate the structural properties of the BHJ and their evolution under operational conditions, both ex situ and operando GISAXS measurements are performed on the PTQ-2F:BTP-4F solar cell films, with the ex situ measurements performed on BHJs on pure Si substrates without additional functional layers to establish baseline insights into the initial morphology of the active layer, uncompromised by interferences from additional layers. The analysis of the scattering patterns is carried out based on horizontal line cuts of the 2D GISAXS data (Figure S2b) taken at the critical angle of the used polymer PTQ-2F, which was measured on a reference pure film of PTQ-2F to be 0.11° at the used X-ray energy of 11.83 keV, thereby maximizing the scattering contribution of PTQ-2F (Figure S2c). BHJs fabricated from the benzene-based solvents CB, *o*XY, and TMB have a significant overlap in the size distributions of the domain radii R_1 and R_2, creating a relatively wide range of medium-sized domains strongly contributing to the overall morphology, whereas a distinguished small-scale domain in the 1–10 nm range can only be determined within CF-processed BHJs. With the relatively large exciton diffusion lengths in PTQ-2F:BTP-4F BHJs, which—depending on device architecture and processing conditions, have been reported to reach 14.8–19 nm and 53.1–330 nm, respectively—these shifts in morphology have little to no impact on the J_{SC} (Figure 1c), as the majority of domains are well within the size limits to allow for good exciton dissociation and charge carrier extraction [27–30]. Rather, a major impacting factor on the PCE of the OSCs produced can be traced to the V_{OC} (Table 1), which is lowered by the altered optoelectronic properties of the BHJs, previously suggested to be a consequence of a higher share of J-type aggregates in the BTP-4F intermolecular structure within active layers produced from CB, *o*XY, or TMB, while also visible in the corresponding BHJ UV–vis spectra (Figure S3) [10, 17, 31–37]. Due to the limited solubility of the active layer materials in the latter solvents at room temperature, the influence of the solvent temperature on the intermolecular orientation of BTP-4F cannot be isolated and thus not be ruled out.

TABLE 1 | Device performance of solar cells produced from various solvents at 100 mW cm^{-2} of illumination with an AM1.5G spectrum. Average values with standard deviations are calculated from the 10 devices with the highest PCE, with the PCE of the champion device given in parentheses. All devices are tested with an illuminated area of at least 7.9 mm^2 defined by a metallic masking sheet.

Solvent	V_{OC}, V	J_{SC}, mA	FF, %	PCE, %
CF	0.86 ± 0.01	21.0 ± 1.5	65 ± 5	11.7 ± 0.3 (12.2)
CB	0.78 ± 0.02	22.0 ± 1.4	58 ± 2	9.9 ± 0.6 (10.5)
*o*XY	0.78 ± 0.02	21.1 ± 2.0	55 ± 3	9.1 ± 0.6 (10.0)
TMB	0.78 ± 0.05	18.1 ± 0.6	63 ± 2	8.9 ± 0.9 (9.9)

2.2 | Operando Study

To understand the kinetic evolution of the BHJ morphology under operational conditions, operando GISAXS measurements are performed under continuous AM1.5G illumination (Figure S4). The OSCs are not encapsulated to observe an accelerated device degradation traceable during the typical available beamtimes of synchrotron radiation facilities. To prevent chemical degradation from atmospheric moisture and oxygen, this measurement is conducted with the OSC placed inside a vacuum chamber, with the incoming and scattered X-rays passing through a thin polyimide window on either side, and the illumination performed through a quartz-glass window from below [38, 39]. GISAXS probing is performed with the active layer locally exposed and thus not covered by the electron blocking layer (EBL) or electrode material, thereby minimizing interferences from these layers (Figure 2a). This also inhibits the use of encapsulation materials, which would be used in realistic applications to counteract additional degradation from ambient environments, though could cause additional degradation pathways on its own. A homogenous illumination of the probed area requires the omission of a masking sheet, typically needed for a precise determination of the illuminated area. *J*–*V* scans are conducted at regular 2 min intervals over 60 min. In comparison, 0.2 s GISAXS measurements are performed at initial 1 min intervals and later 10 min intervals without the area probed by the X-ray beam overlapping in between measurements, thus preventing radiation damage introduced by an overdose of X-ray illumination. Performance degradation kinetics show a stark contrast between OSCs from halogenated solvents compared to those from nonhalogenated solvents (Figure 3b), where the CF and CB films have a gradual decay in PCE over 1 h, whereas *o*XY and TMB show a strong burn-in effect with a rapid decrease in PCE within the first 10 min of illumination, subsequently stabilizing after ca. 30 min of illumination. In all four systems, this performance degradation is mostly driven by a reduction in J_{SC}, especially for OSCs from TMB, where both FF and V_{OC} remain virtually unchanged. The high stability in FF, especially in TMB-processed BHJs, indicates that neither the formation of trap-mediated recombination centers nor photochemical degradation, including from potential residual solvents, significantly contributes to device degradation, as these effects have been reported to coincide with a significant decrease in FF [40–44]. In OSCs from halogenated solvents, we can additionally observe an initial increase in V_{OC}, which slowly decays over time, whereas it remains permanently raised in OSCs from *o*XY, though being counteracted by an equal decrease in FF. However, *o*XY-processed OSCs present a superior PCE retention, dropping by only (30 ± 2)% within 1 h, whereas all other systems already lose between 50% and 60% PCE in the same timeframe.

Equivalently to the analysis performed with ex situ GISAXS measurements, the morphology is modeled with a set of three cylindrical form factors on the horizontal line cuts of the 2D GISAXS data in the Yoneda region of the PTQ-2F polymer (Figure 2b). For the operating time $t = 0$, prior to illumination, this results in a domain size distribution in good agreement with

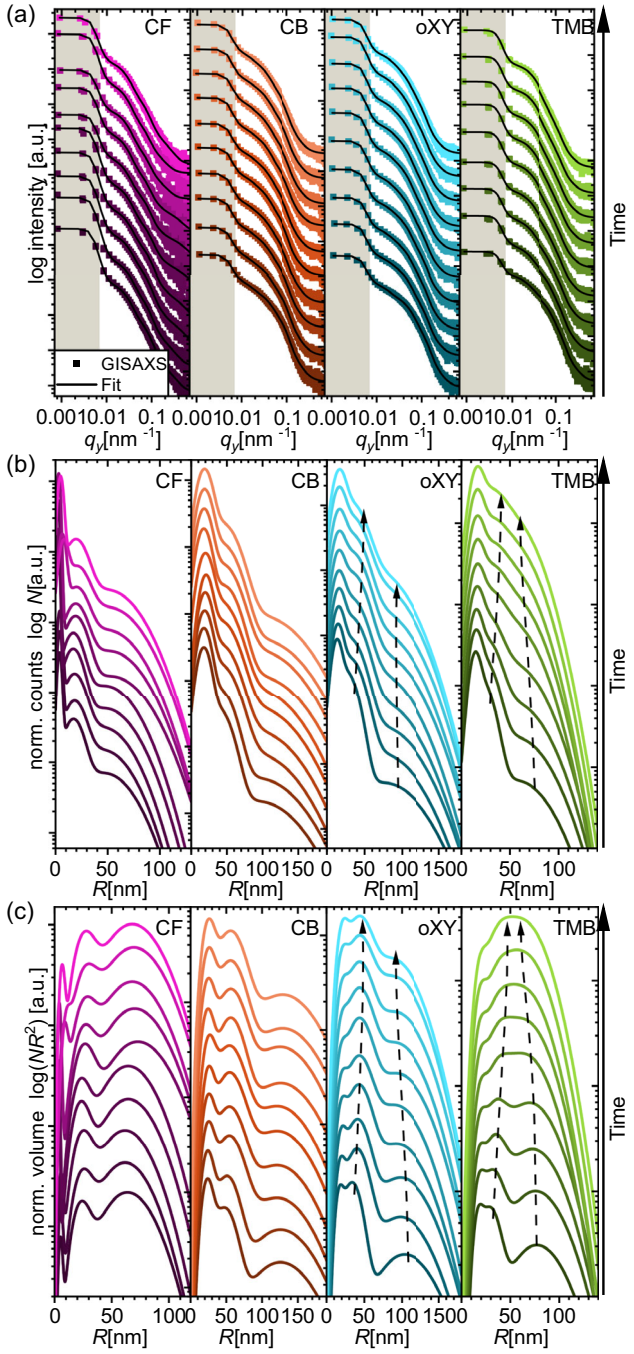

FIGURE 2 | (a) Horizontal line cuts through the Yoneda-region at $q_z = 0.437$ nm^{-1} from operando GISAXS measurements performed on PTQ-2F:BTP-4F OSCs prepared from different solvents, including fits. The resolution limit defined by the beam width is highlighted in gray. (b) Domain size distribution obtained from operando GISAXS fits. (c) Volume-weighted domain size distribution obtained from operando GISAXS fits.

the results obtained from the ex situ GISAXS analysis for all four studied solvents (Figure 2c). We also observe clear alterations of the BHJ morphology over time, whereby the overall kinetics in the change of polymer domain sizes mirror those of the degradation of the respective OSC performance. Thus, BHJs from nonhalogenated solvents undergo rapid morphological changes within the first 10 min of illumination and practically fully stabilize within 30 min, whereas the use of halogenated solvents results in a more gradual change in the morphology (Figure 3a). In CF-processed OSCs, this causes R_1 to grow from $3.8 - 0.7 + 1.1$ to $7.5 - 1.7 + 2.0$ nm, with the growth of R_2 from 17.4 ± 1.8 to 20 ± 2 nm and R_3 from 44 ± 4 to 50 ± 4 nm being much more insignificant. In CB-processed OSCs, outgoing from already initially enlarged domain sizes, we can observe a growth in R_1 from 17.1 ± 1.8 to 17.9 ± 1.8 nm, in R_2 from 37 ± 5 to 43 ± 2 nm, and in R_3 from 93 ± 12 to 96 ± 15 nm. With OSCs from oXY, we can observe an increase in R_1 from 13.0 ± 1.2 to 16.1 ± 2.6 nm and in R_2 from 24.5 ± 1.7 to 31 ± 3 nm, though a contrasting decrease in R_3 from 74 ± 8 to 62 ± 6 nm. Similarly, in TMB-processed OSCs, the growth of R_1 from 14.0 ± 1.7 nm to 16 ± 2 nm and of R_2 from 22 ± 2 to 28 ± 3 nm is accompanied by the shrinkage of R_3 from 55 ± 4 to 44 ± 4 nm.

This growing behavior of BHJ polymer domains was also reported by Wienhold et al. for printed OSCs with NFAs [38], reflecting the coalescing of smaller polymer domains. However, the change in R_i of the different domains alone cannot fully describe the vastly different behavior in performance degradation. For this, the number density N of the individual domain sizes must also be further elucidated. We can find from the normalized count of different scattering domains deduced from the Gaussian distribution of radii that, beyond the growth of the individual domain radii, the relative count of the larger domains, R_2 and R_3, increases as well, to the detriment of R_1. This behavior becomes increasingly relevant, as it enhances the overall growth in domain sizes in the range of several 10 nm, where successful charge carrier extraction becomes increasingly limited by exciton diffusion length, decreasing J_{SC} in the process [45, 46]. However, this process has been typically attributed to a shift in R_2, as it is most commonly in the order of magnitude of the diffusion length [38, 39, 45, 47]. We observe, especially in the case of TMB-processed OSCs, the contribution of R_3 becoming increasingly prominent in number and size after the initial burn-in process. This is even more apparent when looking at the actual volume $V \propto NR^2$ of the respective cylindrical domains (Figure 2c), which is a relevant measure for indicating the amount of material present within a certain domain size regime. Since the charge carrier diffusion length in OSCs is very limited, a large volumetric share in domains larger than the typical diffusion length causes a decrease in the interface-to-volume ratio and thus a strong decline in J_{SC} [48]. The morphological degradation behavior of TMB-processed OSCs starkly contrasts that of *o*XY-processed OSCs, despite their extremely closely matching morphology in their initial state. The merging of small-scale domains, attributed to an increased mobility of the donor and acceptor materials, into larger domains centered around 50–60 nm, strongly depletes the amount of donor material within the limits of the exciton diffusion length of PTQ-2F, matching the observed sharp decrease in J_{SC}. This collapsing behavior cannot be observed in the morphology of the other OSC systems.

Regardless of the superficially similar degradation kinetics in *o*XY-processed OSCs (Figure 3a), the majority of domains remain in a more favorable, smaller size range. Here, the aggregation of domains R_1 and R_2 toward larger radii does not lead to a complete collapse, as in the case of TMB, but instead quickly stabilizes, without R_3 becoming profusely dominant, leading to the comparatively high stability of J_{SC} previously observed. In both systems using nonhalogenated solvents, the decrease of the mean value in R_3 can be the result of this merging of smaller domains, leading to the respective domain size population being skewed toward smaller radii. Such behavior was previously also attributed to

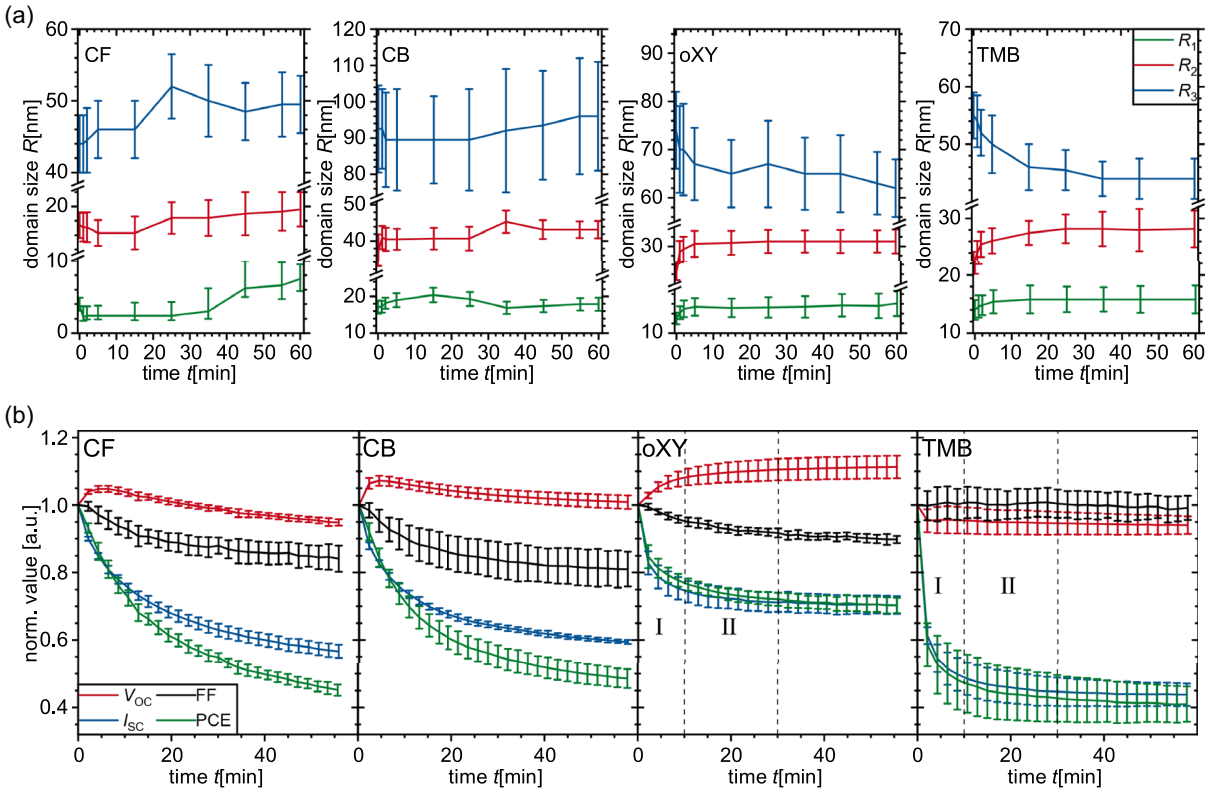

FIGURE 3 | (a) Evolution of domain sizes over time obtained from operando GISAXS fits of PTQ-2F:BTP-4F OSCs prepared from different solvents. (b) Evolution of photovoltaic parameters of PTQ-2F:BTP-4F OSCs during operando GISAXS normalized to the conditions at $t = 0$. Areas labeled with roman numerals I and II indicate the timeframes of initial burn-in and subsequent stabilization, respectively.

the evaporation of residual solvent [39, 47, 49]. However, in this case, the strong similarities of the thermophysical properties of both nonhalogenated solvents (Table S1) are insufficient to explain this difference, as both temperature and vacuum quality during deposition of OSC layers subsequent to the BHJ formation are well in excess of those encountered during operando measurements. Though the presence of residual solvent immediately after drying of the active layer cannot be entirely ruled out, any potential impact on the BHJ morphology due to outgassing or material diffusion under thermal load would occur well in advance of OSC operation and thus not be observable here. In both CF- and CB-processed OSCs, the relative distribution of domain radii remains mostly unchanged, despite their obvious, albeit low, overall growth. Thus, we can suppose that the domain size growth is driven by the phase separation of the intermixed polymer-acceptor phase present in the BHJ, adding comparatively equally to the increase in R_i over all domain sizes [45, 50–53]. Since the BHJ morphology is initially far from a thermodynamic equilibrium state, the domain coarsening through external stresses is highly dependent on the morphological starting conditions. Minute differences in the geometry or aspect ratio of the intermixed phases have been previously suggested to strongly influence the coarsening behavior of the BHJ film [11]. The lack of domains decreasing in size is typical for a nonmixable donor–acceptor blend.

3 | Conclusion

In summary, we show the feasibility of processing PTQ-2F:BTP-4F OSCs from nonhalogenated solvents hitherto considered incompatible with this donor:acceptor system through a hot-solvent process with only a minor reduction in the initial PCE. Ex situ morphological studies performed through GISAXS reveal strong similarities among the domain size distributions of the BHJs processed from benzene-based solvents, setting them apart from typically utilized CF. We also observe a noticeably lowered V_{OC} within OSCs from these solvents, caused by the morphological impact on the optoelectronic properties of the active layer materials. Furthermore, the PCE stability of such produced OSCs is heavily influenced by the solvent used. Halogenated solvents result in gradual degradation kinetics, whereas nonhalogenated solvents facilitate a prominent initial burn-in process with subsequent stabilization of the PCE. As a result, *o*XY-processed OSCs have an improved overall stability over all other tested solvents. Through operando GISAXS, we connect these significant differences in the device degradation kinetics to a respective different behavior in the time evolution of domain sizes within the BHJs. We find a superior stability of *o*XY-based OSCs to result from the limited coalescing of small radii domains, retaining a more small-grained morphology. Our study highlights the importance of the BHJ morphology for developing efficient and stable OSCs and how it is shaped by the choice of processing solvent, even in their absence within the finished, dried BHJ under operation. Our results suggest that *o*XY is a particularly promising nonhalogenated solvent for fabricating OSCs with enhanced stability, potentially paving the way for more sustainable photovoltaic technologies.

Acknowledgments

This work was supported by funding from the Deutsches Zentrum für Luft- und Raumfahrt e.V. (DLR) in the SVALIN project

(FKZ 50WM2256), Deutsche Forschungsgemeinschaft (DFG, German Research Foundation) under Germany's Excellence Strategy – EXC 2089/1 – 390776260 (e conversion) and via International Research Training Group 2022 Alberta/Technical University of Munich International Graduate School for Environmentally Responsible Functional Materials (ATUMS), TUM.solar in the context of the Bavarian Collaborative Research Project Solar Technologies Go Hybrid (SolTech) and the Center for NanoScience (CeNS). J.E.H. acknowledges funding through BMBF FKZ 05D23WO1. The authors acknowledge DESY (Hamburg, Germany), a member of the Helmholtz Association HGF, for the provision of experimental facilities. Operando GISAXS measurements were carried out at PETRA III, and the authors thank Jan Rubeck for assistance in using beamline P03. The authors also thank Lea Westphal for assisting with the ToC figure.

Open Access funding enabled and organized by Projekt DEAL.

Funding

This work was supported by Deutsches Zentrum für Luft- und Raumfahrt e.V. (DLR) (50WM2256), Deutsche Forschungsgemeinschaft (DFG, German Research Foundation) EXC2089/1-390776260 (IRTG2022), Bundesministerium für Forschung, Technologie und Raumfahrt (BMFTR) (05D23WO1) Bayerisches Staatsministerium für Wissenschaft und Kunst, SolTech; Center for NanoScience (CeNS).

Conflicts of Interest

The authors declare no conflicts of interest.

Data Availability Statement

The data that support the findings of this study are available from the following public repository: https://doi.org/10.14459/2026mp1840497.

References

1. J. Hou, O. Inganäs, R. H. Friend, and F. Gao, "Organic Solar Cells Based on Non-Fullerene Acceptors," *Nature Materials* 17 (2018): 119–128.

2. L. Zhu, M. Zhang, J. Xu, et al., "Single-Junction Organic Solar Cells with over 19% Efficiency Enabled by a Refined Double-Fibril Network Morphology," *Nature Materials* 21 (2022): 656–663.

3. J. Gao, N. Yu, Z. Chen, et al., "Over 19.2% Efficiency of Organic Solar Cells Enabled by Precisely Tuning the Charge Transfer State Via Donor Alloy Strategy," *Advanced science* 9 (2022): e2203606.

4. H. Chen, Y. Huang, R. Zhang, et al., "Organic Solar Cells with 20.82% Efficiency and High Tolerance of Active Layer Thickness through Crystallization Sequence Manipulation," *Nature Materials* 24 (2025): 444, https://doi.org/10.1038/s41563-024-02062-0.

5. L. K. Reb, M. Böhmer, B. Predeschly, et al., "Perovskite and Organic Solar Cells on a Rocket Flight," *Joule* 4 (2020): 1880–1892.

6. I. Cardinaletti, T. Vangerven, S. Nagels, et al., "Organic and Perovskite Solar Cells for Space Applications," *Solar Energy Materials and Solar Cells* 182 (2018): 121–127.

7. R. Zhang, H. Chen, T. Wang, et al., "Equally High Efficiencies of Organic Solar Cells Processed from Different Solvents Reveal Key Factors for Morphology Control," *Nature Energy* 10 (2025): 124–134.

8. F. T. A. Wibowo, N. V. Krishna, S. Sinaga, et al., "High-Efficiency Organic Solar Cells Prepared Using a Halogen-Free Solution Process," *Cell Reports Physical Science* 2 (2021): 100517.

9. O. Almora, D. Baran, G. C. Bazan, et al., "Device Performance of Emerging Photovoltaic Materials (Version 3)," *Advanced Energy Materials* 13 (2023): 2203313, https://doi.org/10.1002/aenm.202203313.

10. H. Zhao, H. B. Naveed, B. Lin, et al., "Hot Hydrocarbon-Solvent Slot-Die Coating Enables High-Efficiency Organic Solar Cells with Temperature-Dependent Aggregation Behavior," *Advanced Materials* 32 (2020): e2002302.

11. M. A. Ruderer, S. Guo, R. Meier, et al., "Solvent-Induced Morphology in Polymer-Based Systems for Organic Photovoltaics," *Advanced Functional Materials* 21 (2011): 3382–3391.

12. J. Panidi, E. Mazzolini, F. Eisner, et al., "Biorenewable Solvents for High-Performance Organic Solar Cells," *ACS Energy Letters* 8 (2023): 3038–3047.

13. M. Nuber, L. V. Spanier, S. Roth, et al., "Picosecond Charge-Transfer-State Dynamics in Wide Band Gap Polymer-Non-Fullerene Small-Molecule Blend Films Investigated via Transient Infrared Spectroscopy," *The Journal of Physical Chemistry Letters* 13 (2022): 10418–10423.

14. K. Jin, Z. Xiao, and L. Ding, "18.69% PCE from Organic Solar Cells," *Journal of Semiconductors* 42 (2021): 60502.

15. K. Jiang, Q. Wei, J. Y. L. Lai, et al., "Alkyl Chain Tuning of Small Molecule Acceptors for Efficient Organic Solar Cells," *Joule* 3 (2019): 3020–3033.

16. Y. Cui, H. Yao, J. Zhang, et al., "Single-Junction Organic Photovoltaic Cells with Approaching 18% Efficiency," *Advanced Materials* 32 (2020): e1908205.

17. S. Dong, T. Jia, K. Zhang, J. Jing, and F. Huang, "Single-Component Non-Halogen Solvent-Processed High-Performance Organic Solar Cell Module with Efficiency over 14%," *Joule* 4 (2020): 2004–2016.

18. Y. Cai, Y. Li, R. Wang, et al., "A Well-Mixed Phase Formed by Two Compatible Non-Fullerene Acceptors Enables Ternary Organic Solar Cells with Efficiency over 18.6," *Advanced Materials* 33 (2021): e2101733.

19. R. Szymanski, R. Henry, S. Stuard, et al., "Balanced Charge Transport Optimizes Industry-Relevant Ternary Polymer Solar Cells," *Solar RRL* 4 (2020): 2000538.

20. D. Yuan, F. Pan, L. Zhang, et al., "Improved Average Figure-of-Merit of High-Efficiency Nonfullerene Solar Cells via Minor Combinatory Side Chain Approach," *Solar RRL* 4 (2020): 2000062, https://doi.org/10.1002/solr.202000062.

21. K. S. Wienhold, V. Körstgens, S. Grott, et al., "Effect of Solvent Additives on the Morphology and Device Performance of Printed Nonfullerene Acceptor Based Organic Solar Cells," *ACS Applied Materials & Interfaces* 11 (2019): 42313–42321.

22. H. Chen, R. Zhang, X. Chen, et al., "A Guest-Assisted Molecular-Organization Approach for >17% Efficiency Organic Solar Cells Using Environmentally Friendly Solvents," *Nature Energy* 6 (2021): 1045–1053.

23. H. Tian, W. Xu, Z. Liu, et al., "Over 18.8% Efficiency of Layer-By-Layer Organic Photovoltaics Enabled by Ameliorating Exciton Utilization in Acceptor Layer," *Advanced Functional Materials* 34 (2024): 2313751, https://doi.org/10.1002/adfm.202313751.

24. H. Zhou, Y. Sun, M. Zhang, et al., "Over 18.2% Efficiency of Layer-by-Layer All-Polymer Solar Cells Enabled by Homoleptic Iridium(III) Carbene Complex as Solid Additive," *Science Bulletin* 69 (2024): 2862–2869.

25. Q. Zhu, J. Xue, G. Lu, et al., "Efficient and Mechanically-Robust Organic Solar Cells Based on Vertical Stratification Modulation through Sequential Blade-Coating," *Nano Energy* 97 (2022): 107194.

26. D. Corzo, D. Rosas-Villalva, C. A., et al., "High-Performing Organic Electronics Using Terpene Green Solvents from Renewable Feedstocks," *Nature Energy* 8 (2023): 62–73.

27. C. Chen, G. Wen, Z. Xiao, et al., "Charge Photogeneration and Recombination Dynamics in PTQ10: Y6 Solar Cells," *Photonics* 9 (2022): 892.

28. C. J. Schaffer, J. Schlipf, E. Dwi Indari, B. Su, S. Bernstorff, and P. Müller-Buschbaum, "Effect of Blend Composition and Additives on the Morphology of PCPDTBT: PC71BM Thin Films for Organic Photovoltaics," *ACS Applied Materials & Interfaces* 7 (2015): 21347–21355.

29. H. Cha, Y. Zheng, Y. Dong, et al., "Exciton and Charge Carrier Dynamics in Highly Crystalline PTQ10: IDIC Organic Solar Cells," *Advanced Energy Materials* 10 (2020): 2001149.

30. N. Tokmoldin, S. M. Hosseini, M. Raoufi, et al., "Extraordinarily Long Diffusion Length in PM6: Y6 Organic Solar Cells," *Journal of Materials Chemistry A* 8 (2020): 7854–7860.

31. N. J. Hestand and F. C. Spano, "Expanded Theory of H- and J-Molecular Aggregates: The Effects of Vibronic Coupling and Intermolecular Charge Transfer," *Chemical Reviews* 118 (2018): 7069–7163.

32. D. Kroh, F. Eller, K. Schötz, et al., "Identifying the Signatures of Intermolecular Interactions in Blends of PM6 with Y6 and N4 Using Absorption Spectroscopy," *Advanced Functional Materials* 32 (2022): 2205711, https://doi.org/10.1002/adfm.202205711.

33. G. Kupgan, X. K. Chen, and J. L. Brédas, "Molecular Packing of Non-Fullerene Acceptors for Organic Solar Cells: Distinctive Local Morphology in Y6 vs. ITIC Derivatives," *Materials Today Advances* 11 (2021): 100154.

34. X. Jiang, P. Chotard, K. Luo, et al., "Revealing Donor–Acceptor Interaction on the Printed Active Layer Morphology and the Formation Kinetics for Nonfullerene Organic Solar Cells at Ambient Conditions," *Advanced Energy Materials* 12 (2022): 2103977, https://doi.org/10.1002/aenm.202103977.

35. Z. Aliakbar Tehrani and K. S. Kim, "Functional Molecules and Materials by π-Interaction Based Quantum Theoretical Design," *International Journal of Quantum Chemistry* 116 (2016): 622–633.

36. O. Ostroverkhova, "Organic Optoelectronic Materials: Mechanisms and Applications,," *Chemical Reviews* 116 (2016): 13279–13412.

37. Q. Zhao, H. Lai, H. Chen, H. Li, and F. He, "H- and J-Aggregation Inspiring Efficient Solar Conversion," *Journal of Materials Chemistry A* 9 (2021): 1119–1126.

38. K. S. Wienhold, W. Chen, S. Yin, et al., "Following in Operando the Structure Evolution-Induced Degradation in Printed Organic Solar Cells with Nonfullerene Small Molecule Acceptor," *Solar RRL* 4 (2020): 2000251.

39. C. J. Schaffer, C. M. Palumbiny, M. A. Niedermeier, et al., "Morphological Degradation in Low Bandgap Polymer Solar Cells – An In Operando Study," *Advanced Energy Materials* 6 (2016): 1600712, https://doi.org/10.1002/aenm.201600712.

40. C. H. Peters, I. T. Sachs-Quintana, W. R. Mateker, et al., "The Mechanism of Burn-in Loss in a High Efficiency Polymer Solar Cell," *Advanced Materials* 24 (2012): 663–668,

41. M. B. Upama, M. Wright, M. A. Mahmud, et al., "Photo-Degradation of High Efficiency Fullerene-Free Polymer Solar Cells," *Nanoscale* 9 (2017): 18788–18797.

42. W. Kim, J. K. Kim, E. Kim, T. K. Ahn, D. H. Wang, and J. H. Park, "Conflicted Effects of a Solvent Additive on PTB7: PC. 71 BM Bulk Heterojunction Solar Cells," *Journal of Physical Chemistry C* 119 (2015): 5954–5961.

43. W. Li, D. Liu, and T. Wang, "Stability Of Non-Fullerene Electron Acceptors and Their Photovoltaic Devices," *Advanced Functional Materials* 31 (2021): 2104552, https://doi.org/10.1002/adfm.202104552.

44. T. Liu, Q. C. Burlingame, M. R. Ivancevic, et al., "Photochemical Decomposition of Y-Series Non-Fullerene Acceptors Is Responsible for Degradation of High-Efficiency Organic Solar Cells," *Advanced Energy Materials* 13 (2023): 2300046, https://doi.org/10.1002/aenm.202300046.

45. P. Müller-Buschbaum, "The Active Layer Morphology of Organic Solar Cells Probed with Grazing Incidence Scattering Techniques," *Advanced Materials* 26 (2014): 7692–7709.

46. C. Fan and Z. Zhao, eds. *Synchrotron Radiation in Materials Science* (Wiley, 2018).

47. Z. Li, Y. Li, J. Zhang, et al., "Suppressed Degradation Process of Green-Solvent Based Organic Solar Cells Through ZnO Modification With Sulfhydryl Derivatives," *Advanced Energy Materials* 15 (2024): 2402920, https://doi.org/10.1002/aenm.202402920.

48. C. J. Schaffer, C. M. Palumbiny, M. A. Niedermeier, et al., "A Direct Evidence of Morphological Degradation on a Nanometer Scale in Polymer Solar Cells," *Advanced Materials* 25 (2013): 6760–6764,

49. D. Yang, F. C. Löhrer, V. Körstgens, et al., "In-Operando Study of the Effects of Solvent Additives on the Stability of Organic Solar Cells Based on PTB7-Th: PC. 71 BM," *Acs Energy Letters* 4 (2019): 464–470.

50. D. Chen, F. Liu, C. Wang, A. Nakahara, and T. P. Russell, "Bulk Heterojunction Photovoltaic Active Layers via Bilayer Interdiffusion," *Nano Letters* 11 (2011): 2071–2078.

51. B. A. Collins, E. Gann, L. Guignard, X. He, C. R. McNeill, and H. Ade, "Molecular Miscibility of Polymer−Fullerene Blends," *The Journal of Physical Chemistry Letters* 1 (2010): 3160–3166.

52. M. A. Ruderer, R. Meier, L. Porcar, R. Cubitt, and P. Müller-Buschbaum, "Phase Separation and Molecular Intermixing in Polymer-Fullerene Bulk Heterojunction Thin Films," *Journal of Physical Chemistry Letters* 3 (2012): 683–688.

53. N. D. Treat, M. A. Brady, G. Smith, et al., "Interdiffusion of PCBM and P3HT Reveals Miscibility in a Photovoltaically Active Blend," *Advanced Energy Materials* 1 (2011): 82–89.

54. A. Buffet, A. Rothkirch, R. Döhrmann, et al., "P03, the Microfocus and Nanofocus X-Ray Scattering (MiNaXS) Beamline of the PETRA III Storage ring: The Microfocus Endstation," *Journal of Synchrotron Radiation* 19 (2012): 647–653.

55. G. Benecke, W. Wagermaier, C. Li, et al., "A Customizable Software for Fast Reduction and Analysis of Large X-Ray Scattering Data Sets: Applications of the New DPDAK Package to Small-Angle X-Ray Scattering and Grazing-Incidence Small-Angle X-Ray Scattering," *Journal of Applied Crystallography* 47 (2014): 1797–1803.

56. Z. Jiang, "GIXSGUI : A MATLAB Toolbox for Grazing-Incidence X-Ray Scattering Data Visualization and Reduction, and Indexing of Buried Three-Dimensional Periodic Nanostructured Films," *Journal of Applied Crystallography* 48 (2015): 917–926.

57. T. A. Ezquerra, *Applications of Synchrotron Light to Scattering and Diffraction in Materials and Life Sciences* (Springer, 2009).

58. G. Pan, S. Yin, L. F. Huber, et al., "UV Irradiation as a Versatile Low-Temperature Strategy for Fabricating Templated Mesoporous Titania Films," *Small* 21 (2024): e2409856.

59. J. Zhang, Z. Li, X. Jiang, et al., "Revealing the Effect of Solvent Additive Selectivity on Morphology and Formation Kinetics in Printed Non-Fullerene Organic Solar Cells at Ambient Conditions," *Advanced Energy Materials* 15 (2024): 2404724, https://doi.org/10.1002/aenm.202404724.

60. R. Lazzari, F. Leroy, and G. Renaud, "Grazing-Incidence Small-Angle X-Ray Scattering from Dense Packing of Islands on Surfaces: Development of Distorted Wave Born Approximation and Correlation between Particle Sizes and Spacing," *Physical Review. B* 76 (2007): 125411, https://doi.org/10.1103/PhysRevB.76.125411.

61. D. R. Stull, "Vapor Pressure of Pure Substances. Organic and Inorganic Compounds," *Industrial and Engineering Chemistry* 39 (1947): 517–550.

62. I. Brown, "Liquid-Vapour Equilibria. III. The Systems Benzene-n-Heptane, n-Hexane-Chlorobenzene, and Cyclohexane-Nitrobenzene," *Australian Journal of Scientific Research Series A* 5 (1952): 530–540.

63. C. B. Willingham, W. J. Taylor, J. M. Pignocco, and F. D. Rossini, "Vapor Pressures and Boiling Points of Some Paraffin, Alkylcyclopentane, Alkylcyclohexane, and Alkylbenzene Hydrocarbons," *Journal of Research of the National Bureau of Standards* 35 (1945): 219.

64. A. F. Forziati, W. R. Norris, and F. D. Rossini, "Vapor Pressures and Boiling Points of Sixty API-NBS Hydrocarbons," *Journal of Research of the National Bureau of Standards* 43 (1949): 555.

65. J. Puvipirom and S. Chaiseri, "Contribution of Roasted Grains and Seeds in Aroma of Oleang (Thai Coffee Drink)," *International Food Research Journal* 19 (2012): 583–588.

66. J. J. Dowling, M. B. Evans, and J. K. Haken, "Gas—liquid Chromatography in Qualitative Analysis," *Journal of Chromatography A* 500 (1990): 355–365.

67. L. Sun, J. I. Siepmann, W. L. Klotz, and M. R. Schure, "Retention in Gas-Liquid Chromatography with a Polyethylene Oxide Stationary Phase: Molecular Simulation and Experiment," *Journal of Chromatography A* 1126 (2006): 373–380.

68. D. I. Papazova and M. C. Pankova, "Identification of Individual Aromatic Hydrocarbons in Kerosene Fraction (b.p. 150°-250°)," *Journal of Chromatography A* 105 (1975): 411–414.

69. J. Neu, J. Oh, S. Mukherjee, et al., "Tuning the Solubility Parameters of Conjugated Polymers via Side-Chain Engineering for All-Polymer Solar Cells," *Chemistry of Materials* 37 (2025): 3788–3798.

70. L. P. Christopholi, C. F. N. Marchiori, I. Jalan, A. Opitz, S. A. Muntean, and E. Moons, "Role of the Solvent on the Orientation of Y-Type Acceptor Molecules in Spin-Coated Films," *Journal of Physical Chemistry C* 128 (2024): 17825–17835.

71. A. Steven, M. H.Charles, and Y. Hiroshi, *Hansen Solubility Parameters in Practice. Complete with Software, Data and Examples, Hansen-Solubility.com*, 5th ed. (2015), eBook: ISBN: 9780955122026. Available from www.hansen-solubility.com.

72. L. Ito, T. Fujii, N. Fujiwara, S. Watanabe, K. Toyoda, and H. Yamamoto, "Predictive Study of Eye Irritation Results Obtained from the STE Method Using Hansen Solubility Parameters," *Jouranal of Society Cosmetic Chemists Japan* 56 (2022): 53–59.

Supporting Information

Additional supporting information can be found online in the Supporting Information section. Additional references are cited in the Supporting Information [54–72]. **Supporting Fig. S1:** Operando solar cell measurement setup as installed at PETRA III P03 beamline (DESY) with important components highlighted. **Supporting Fig. S2:** a) *Ex situ* 2D GISAXS data of PTQ-2F:BTP-4F BHJs prepared from different solvents on Si substrates, with the location of the horizontal line cut highlighted as a dashed line. b) Horizontal line cuts through the Yoneda-region at $q_z = 0.437\ nm^{-1}$ from GISAXS measurements of PTQ-2F:BTP-4F BHJs on Si including fits. The gray area indicates the resolution limit. c) Off-center vertical line cut of PTQ-2F thin films with the Yoneda-Peak highlighted. The gray area indicates a detector gap. d) Domain size distribution obtained from GISAXS fits of PTQ-2F:BTP-4F BHJs on Si. e) Volume-weighted domain size distribution obtained from these GISAXS fits. **Supporting Fig. S3:** UV-Vis absorption spectra of PTQ-2F:BTP-4F BHJ films on glass substrates. The blue shift of the peak position of 0-0 transition in BTP-4F with films produced from CF solution is highlighted separately. **Supporting Fig. S4:** Schematic depiction of operando GISAXS setup. The OSC is illuminated from the bottom while the GISAXS measurement probes an area uncovered by the blocking layer in between the electrodes. **Supporting Fig. S5:** Time evolution as a waterfall graph of volume-weighted domain size distribution obtained from operando GISAXS on OSCs processed from a) CF, b) CB, c) oXY, and d) TMB. **Supporting Table S1:** Thermophysical properties of solvents used. **Supporting Table S2:** PTQ-2F domain sizes from *ex situ* GISAXS analysis. **Supporting Table S3:** Hansen solubility parameters of materials used under ambient conditions.